Re-examining flow pathways over the Chukchi Sea continental shelf

Phyllis J. Stabeno[1], Ryan M. McCabe[2],

[1]NOAA Pacific Marine Environmental Laboratory
7600 Sand Point Way NE
Seattle WA 98115-0070
Phone: (206) 526-6453
Fax: (206) 526-6485
Phyllis.stabeno@noaa.gov

[2]NOAA Pacific Marine Environmental Laboratory
7600 Sand Point Way NE
Seattle WA 98115-0070

For submission to AIERP Special Issue 2

Deep Sea Research

December 5, 2022

Abstract:
Velocity records from 8 mooring sites (2010–2019) and trajectories of drogued drifters (2012–2020) are used to evaluate patterns of flow on the Chukchi Sea continental shelf, with an emphasis on the latter three years (2016–2019). Together, these data provided insight into the temporal and spatial variability of the currents over this shelf. These data extend previous observations by five years and include three previously unoccupied sites, two of which span the Central Channel. Bathymetry directs a significant portion of the northward flow in Central Channel eastward across the Chukchi shelf where it joins the coastal flow prior to exiting Barrow Canyon and entering the Beaufort Sea. In addition, shelf-wide volume transport estimated from three mooring sites located off Icy Cape is modified from earlier analysis and extended in time to a decade. The resulting transport is highly correlated with that flowing through Central Channel, with similar magnitude. Icy Cape transport varies seasonally with variations in atmospheric forcing, as well as inter-annually, with an annual low of 0.24 Sv (September 2011 – August 2012) to 0.64 Sv (September 2017 – August 2018), and a 9-year average of 0.43 Sv, or approximately 40% of the flow through Bering Strait. This nearly decade-long Icy Cape volume transport record also exhibits an increasing, although not significant, trend of ~0.03 Sv/year.

Key words: Chukchi Sea, currents, transport, winds, Alaskan Coastal Current

1. Introduction

The Chukchi Sea consists of a broad, shallow (<80 m) shelf, extending >800 km northward from its southern boundary at Bering Strait to the shelf break bounding the Arctic basin (Fig. 1). The flow on the shelf is generally northward, following bathymetry. This northward transport largely originates at Bering Strait where ~1 × 10^6 m^3 s^{-1} (1 Sverdrup [Sv]) of Pacific water enters the Chukchi from the eastern Bering Sea shelf (Woodgate et al., 2005a, 2005b, 2012). Most of this flow exits the Chukchi shelf through two canyons—Barrow Canyon in the east (Coachman et al., 1975; Weingartner et al., 2005) and Herald Canyon in the west (Coachman et al., 1975; Pickart et al., 2010). While some of the flow exiting Herald Canyon enters the basin, there is a relatively narrow south-eastward flowing shelfbreak jet centered near the 80-m isobath (Corlett and Pickart, 2017; Li et al., 2019). The northwestward flow along the slope, confined to the upper 200–300 m of the water column, is the Chukchi Slope Current (Corlett and Pickart, 2017; Stabeno et al., 2018; Li et al., 2019; Stabeno and McCabe, 2020). The flow exiting the Chukchi shelf *via* Barrow Canyon is primarily the Alaskan Coastal Current (northward flow through Central Channel that joins the coastal flow offshore of Icy Cape), with a small contribution from the eastward flow along the shelf break (~80 m depth).

Upon exiting Barrow Canyon the more shallow coastal water turns eastward and flows along the Alaskan coast, while the deeper water in the canyon enters the basin and turns westward joining the Chukchi Slope Current (Stabeno and McCabe, 2020). Lin et al. (2021) discuss how changes in wind modulate the flow emanating from Barrow Canyon. The water flowing northward through Barrow Canyon is denser than the surface water in the Beaufort Basin, so as it transits Barrow Canyon the water sinks to a depth of ~60 m (Stabeno et al., 2018; Stabeno and McCabe, 2020; Shroyer and Pickart, 2019). This water is an important source of heat to the subsurface basin (Watanabe et al., 2017).

The Chukchi shelf is generally referred to as an inflow shelf for the Arctic (Carmack and Wassman, 2006), and is the only source of Pacific-origin water to the Arctic Ocean. It is a major source of heat (Watanabe et al., 2017; Tsukada et al., 2018; Danielson et al. 2020), nutrients (Danielson et al., 2017; Mordy et al., 2020), salt, and freshwater (Itoh et al., 2013) to the Arctic. Transport through Bering Strait and through

Barrow Canyon varies on synoptic, annual and decadal time scales. The synoptic variability is driven by local winds, while annual variability is driven by basin-scale adjustments to the wind (Danielson et al., 2014). A recent multi-year increase in transport is related to an increase in the Pacific-Arctic pressure difference (Woodgate, 2018). It is estimated that the amount of flow through the transect at Icy Cape is ~40% of the transport through Bering Strait (Stabeno et al., 2018).

This paper utilizes nine years of current velocity observations on the Chukchi continental shelf, with an emphasis on three recent years of current data collected at eight mooring sites, ranging from a site off Point Hope in the south to a site near the mouth of Barrow Canyon in the north (Fig. 1). Yearlong moorings were deployed consecutively at each site in the summers of 2016, 2017 and 2018. A primary goal of these deployments was to better understand the patterns and magnitude of flow on the US Chukchi shelf. Data sources and data handling methods are described in section 2. Results are presented in section 3, including: a basic description of regional winds, mean flow patterns from moored current meters and from drogued drifters, and spatial relationships among current meter records and winds. We then turn to a more detailed examination of bathymetry and its relationship to a persistent current feature observed on the middle of the Chukchi shelf, where water from Central Channel turns eastward and flows toward Barrow Canyon. Finally we provide an estimate of volume transport in Central Channel and its relationship to an updated estimate of shelf-wide transport past Icy Cape. In doing so, the Icy Cape volume transport estimate is extended in time to nine years. Section 4 provides a discussion and summary of the results and conclusions.

2 Data sources and methods

2.1 Bathymetry

The primary bathymetry data used throughout this paper are the Alaska Region Digital Elevation Model version 2.0 (ARDEMv2.0; Danielson et al., 2015). Other relevant bathymetric data sets are briefly discussed as necessary in the text.

2.2 Atmospheric variables

The European Centre for Medium-Range Weather Forecasts (ECMWF) ERA5 reanalysis (https://climate.copernicus.eu/climate-reanalysis; Hersbach et al., 2020) is a recent update to the ERA-Interim reanalysis (Dee et al., 2011). The ERA5 model has numerous improvements relative to ERA-Interim and includes hourly output at 31-km horizontal resolution. While there is no complete validation of ERA5 in the Alaskan Arctic, Lindsay et al. (2014) found that ERA-Interim was among the top-performing models for a number of key parameters in the region. For 10-m winds, ERA-Interim had low biases (≤ 0.5 m s^{-1}) and the highest correlations (≥ 0.85) among seven different reanalysis models when compared to daily averaged wind records at drifting ice stations (Lindsay et al., 2014). Belmonte Rivas and Stoffelen (2019) document improvements of ERA5 wind relative to ERA-Interim on a global scale, including a 20% improvement in root mean square wind speed agreement with scatterometer winds, and reductions in divergence and curl biases. Given the model and resolution improvements of ERA5 relative to ERA-Interim, we expect model skill to be at least comparable with that of ERA-Interim in the Arctic. Note that a recent comparison of ERA5 10-m winds to those recorded at the Barrow Atmospheric Baseline Observatory near Utqiaġvik, Alaska, between 2014–2017 found high vector correlations ($r = 0.94$) with only a 4° clockwise rotation (Stabeno and McCabe, 2020).

Given the reported favorable comparisons with observations we proceed using ERA5 wind. Data spanning 2010–2020 were downloaded and then linearly interpolated onto desired locations or averaged over specific regions as discussed in the text.

2.3 Moorings

Velocity records from a number of moorings deployed on the Chukchi Sea continental shelf are presented. Moorings included Aanderaa single-point recording current meters (RCM; either RCM 9 or SeaGuard), and an upward looking 300 or 600 kHz acoustic Doppler current profiler (ADCP). Mooring bottom depths are listed in Table 1; current meter instrument depths were typically 5–6 m above the bottom. Other instruments were also deployed on these moorings (e.g., a Sea-Bird Electronics Microcat [SBE37] or SeaCat [SBE19], instruments measuring ice draft depth, fluorescence, nitrate, and oxygen), but those data are not presented in this paper. The

reader is instead referred to Stabeno et al. (2020), Sullivan and Stabeno (this issue, 2022) and Mordy et al. (2021).

All instruments were calibrated prior to deployment and data were processed according to manufacturers' specifications. Current meter time series were low-pass filtered with a 35 h, cosine-squared, tapered Lanczos filter to remove tidal and higher-frequency variability, and then resampled at 6 h intervals. Final processed time series data are accurate to at least ±0.002 °C, ±0.0005 S/m and ±0.5 cm s^{-1} (temperature, conductivity and currents, respectively).

2.4 Satellite-tracked drifters

From 2012 to 2020, the National Oceanographic and Atmospheric Administration's Ecosystems and Fisheries-Oceanography Coordinated Investigations (NOAA EcoFOCI) Program deployed 47 satellite-tracked drifters in the Chukchi Sea or northern Bering Sea. Drifters were drogued at a depth of 25–35 m using a 10-m long "holey sock" drogue. Each drifter reported position and sea surface temperature (SST) *via* Argos ~14 times per day. Data were examined and spurious points were removed by inspection, as were data collected after drogues were lost (as indicated by a sensor), and after drifters grounded or entered into ice (determined from satellite maps of sea-ice extent). The resulting data were linearly interpolated to hourly intervals and low-pass filtered (25-h running mean).

Lagrangian velocities were determined by centered differences of the hourly drifter positions. Spatially gridded mean velocities were also calculated following Stabeno and Reed (1994) and Stabeno et al. (2016b). In this analysis each 2-day period within a grid area was considered an independent estimate. Each rectangular grid cell was 1° latitude × 3° longitude. In addition, three rhomboids of a similar size abutted the slope (as in Stabeno and McCabe, 2020).

3 Results and Discussion

3.1 Meteorology

On average, winds over the eastern Chukchi Sea continental shelf blow southward or southwestward against the mean northward progression of ocean currents that deliver

Pacific-origin water to the Arctic (Fig. 2). The 11-year mean vectors indicate that winds blow predominantly along the Alaskan coast. The annual average was dominated by winter winds; winds tend to weaken during the ice-free summer months and were northward in the northern Bering Sea and near Bering Strait during July. By September or October of any given year, mean winds begin to strengthen again, becoming strongly south-southwestward in December and January.

Annually from 2010–2019, complex (vector) correlations of 10-m ERA5 winds illustrate that winds over a large portion of the Chukchi Sea shelf and even the western Beaufort Sea shelf were highly correlated (amplitudes >0.7) with only small directional differences (<5 °; Fig. 3). ERA5 wind correlation amplitudes were >0.5 over the entire Chukchi Sea, falling below that level only near Bering Strait and the Siberian mainland. These significant correlations are not too surprising given that atmospheric length scales are large, often hundreds of kilometers (e.g., Danielson et al., 2014). Bering Strait, the southern boundary of the Chukchi Sea, is situated ~500 km south of the central Chukchi Sea, near the limit of such scales. These findings are consistent with the analysis by Danielson et al. (2014) who showed that winds near Bering Strait were statistically different from winds over the central Chukchi Sea, and that for periods < 4 days, winds over the central Chukchi shelf were incoherent with winds farther south over the central Bering Sea shelf (near 169°W, 60.3°N).

Complex correlation magnitudes of ERA5 winds during only the winter months (December through March; DJFM) did not vary considerably from those calculated annually (Figs. 3, 4). Correlations calculated over summer, however, showed substantial differences, with the two most extreme cases illustrated in Figure 4. This is also not surprising since winds are typically weakest in summer. Summer 2018 exhibited high correlation magnitudes ($r > 0.7$) over the largest spatial extent. At that time, the entire Chukchi Sea and much of the Beaufort continental shelf had correlations > 0.5. In contrast, summer 2019 had a much more restricted areal extent of high correlations, though all but one of the mooring sites discussed here (C12 southwest of Point Hope) were within the 0.5 correlation amplitude contour. ERA5 summer wind directions over much of the Chukchi shelf nevertheless remained within 5°, particularly in the region spanned by the mooring array.

The high correlations of ERA5 winds spanning mooring sites on the Chukchi continental shelf suggest that winds evaluated at a single central location should be reasonably representative of winds at the mooring sites considered herein as well as throughout much of the Chukchi Sea in general.

3.2 Satellite-tracked drifters

Drifter trajectories from the 47 drifters deployed during 2012–2019 are shown in blue (Fig. 5a). Some of the drifters were deployed south of 69°N, but most of the drifters were deployed in Central Channel and in the vicinity of the moorings off Icy Cape. This resulted in the highest density of trajectories occurring over the eastern Chukchi shelf. Of the drifters deployed south of 69°N, ~60% continued westward toward Herald Canyon, with the rest turning up Central Channel except for one (green, Fig. 5a). It turned southward and joined the Siberian Coastal Current, entering Bering Strait before it lost its drogue. Recall that the drogue depth on each drifter was 25–35 m, so the trajectories are representative of the flow patterns below the surface mixed layer. The flow patterns remain seasonally biased, however, since only trajectories from drifters in ice-free months (July–October) are used.

To help elucidate flow strength and direction, mean Lagrangian velocities (calculated in 1° latitude by 3° longitude boxes on the shelf and rhomboids along the slope) are included as vectors in Figure 5a. The vectors fall into two groups: red vectors represent velocities with at least 8 independent estimates whereas black arrows correspond to averages with fewer than 8 estimates. Several patterns are evident in the trajectories. Flow enters the Chukchi Sea through Bering Strait. Approximately half of drifters turn northward at Central Channel and the others continue westward toward Herald Canyon. This latter flow is slow (<5 cm s^{-1}) and ice arrives before most of these drifters reach Herald Canyon. As stated earlier, most of the drifters were advected northward, up Central Channel and turned eastward near the Icy Cape transect. Drifters did not enter onto Hanna nor Herald Shoals, since both shoals are shallow (< 30 m). It is also clear that the strongest flows exist in Barrow Canyon. The Chukchi Slope Current appears as the strong, northwestward flow clearly evident along the slope (Stabeno and McCabe, 2020).

The mean near-bottom currents measured at the moorings (Fig. 5b) show a flow pattern that is strikingly similar to that described by the drifter trajectories. The vectors derived from the current meters are not limited to the ice-free period, but represent year round flow. Once again, the strongest flow is in Barrow Canyon and the weakest is to the west and north of Hanna Shoal. Velocity observations from these moorings are discussed in further detail in the sections that follow.

3.3 Moorings

In total, the NOAA EcoFOCI Program has occupied 12 mooring sites on the Chukchi shelf and slope. We will present results from all the moorings, but our focus here is on the three-year period (August 2016 – August 2019) when eight moorings (Table 1; C1, C2, C3, C4, C5, C10, C11 and C12) were deployed and all successfully collected current velocity data.

3.3.1 Velocity vertical structure

Shown in Figure 6 are the net speed and direction as a function of depth at each of the mooring sites from mid-August 2018 through mid-August 2019. The results from the other two deployment periods (2016–2017 and 2017–2018) were similar. Note that while the x-axis varies from site to site, the aspect ratios remain constant. Velocity at the northernmost moorings (C1–C5) appears similar, with the strongest flow near the bottom. This is likely a result of the southwestward winds that weaken (and at times, reverse) the near-surface flows. The southern group of moorings has slightly different patterns with stronger flow near the surface, likely because the wind does not oppose the currents. Rotation as a function of depth is relatively small (< 25°) and progresses clockwise with increasing depth as expected. The bottom flow is along the bathymetry (Fig. 5b).

3.3.2 Velocity time series

Annual velocity time series for each of the moorings and the winds over the central Chukchi Sea are illustrated in Figures 7, 8, and 9. The velocity time series are clearly well correlated from site to site (discussed below). The northernmost near-coast moorings at the head of Barrow Canyon (C4 and C5) exhibit the largest velocities, >10

cm s^{-1} average over all deployments (Table 1). At times these flows can be exceedingly large. The largest mean daily flow (132 cm s^{-1}) was observed in summer of 2019 at C5. Over the central Chukchi Sea, current strength decreases offshore as seen in the records from moorings C1, C2 and C3. Velocities measured at the two moorings in Central Channel (C10 and C11) are also highly correlated with each other (discussed below), and there is an overall good correspondence between the currents measured southwest of Point Hope (C12) and those at the other sites. Note that the principal axis of variation was generally in the same direction as the net direction at each of the sites.

The mean pattern of flow mapped out in Figure 5 is clear. Water proceeds northward past Point Hope some of which continues northeastward along the coast toward Barrow Canyon. Another branch proceeds north through Central Channel and eventually turns east to later converge with the coastal flow at Icy Cape. As described previously this northward progression of water is largely driven by the Pacific-Arctic pressure head difference (e.g., Woodgate et al. 2005b; Danielson et al. 2014). Considering Figure 2, it is evident that this pressure gradient force typically overrides the influence of the mean wind. Nevertheless, many of the variations in the currents are clearly related to local winds over the Chukchi Sea (Figs. 7–9). Similarly, it is evident that the weakest northward along-shelf currents and southward reversals tend to follow periods of sustained southwestward winds. Strong northward currents usually follow strong northward wind events.

3.3.3 Wind-current correlations

Lagged complex correlations between ERA5 winds and observed near-bottom currents at each of the moorings deployed in 2016–2018 are provided in Table 2. All correlations were significant ($0.4 < r < 0.7$; $p < 0.1$) with local winds leading currents by 7–17 hours, in agreement with prior studies (e.g., Woodgate et al., 2005b; Stabeno et al., 2018). Correlation angles were usually negative, meaning that the deepest measured currents were directed clockwise, or to the right, of the local wind vector. When correlation angles were positive, the values were often small (≤7°). The exception to this was mooring C12, located southwest of Point Hope (Fig. 1). There, currents were directed ~40° to the left of local winds. This is likely due to the complex bathymetry at

this location - currents appear to follow the nominal direction of the steep bathymetry past Point Hope, consistent with the trajectories of multiple drogued drifters that have transited the region (Fig. 3). The wind-current complex correlations at moorings C1–C5 are consistent with those reported by Stabeno et al. (2018) for NARR winds. That study found similar correlation amplitudes, directional differences, and lags as reported in Table 2 at those mooring locations from 2010–2015.

3.3.4 Current-current correlations

Zero-lag complex correlations among the mooring sites for near-bottom currents are presented in Table 3. Here too, results, similar to those reported by Stabeno et al. (2018), are evident (see their Fig. 2b), indicating that currents over the shelf are well correlated over large spatial scales (>300 km, Weingartner et al., 2005). In particular, lower water column currents at the three moorings closest to the coast (C1, C4, C5) were highly correlated ($r \geq 0.78$; $p < 0.01$) in all three deployment years. Stabeno et al. (2018) also found correlations to be high among the three moorings spanning the transect off Icy Cape (C1, C2, C3), with typical values of ~0.82 between C1 and C2, and ~0.7 between C2 and C3. Our 2017 and 2018 deployments give similar results, but some of the records that began in 2016 are significantly ($p < .01$) lower (e.g., $r = 0.54$ for C1 and C2). The likely cause of this is that in 2016, the C1 ADCP failed. We used currents measured by an Aanderaa RCM that was positioned below the ADCP and thus a few meters closer to the bottom than the deepest ADCP bin. We expect this instrument and depth difference explains most of the 2016 discrepancy at C1.

Results for three moorings sites (C10, C11, and C12), which were not previously occupied, also appear in Table 3. Notably, currents at C10 and C11 were moderately correlated ($0.50 \leq r \leq 0.80$) with the currents at C1–C5, but had much higher correlations ($0.87 \leq r \leq 0.92$) with each other. These two moorings were deployed near the eastern and western edges of Central Channel in ~47 m of water, thus permitting an estimate of transport through the Central Channel (see section 3.5.2). Currents measured at C12, southwest of Point Hope, had the lowest correlation magnitudes with the other moorings ($0.24 \leq r \leq 0.70$). This is not too surprising since this mooring was sited reasonably far (>220 km) from the other moorings. Recall that wind correlation magnitudes between

C12 and the mooring sites over the central Chukchi shelf were significantly weaker (Figs. 3, 4). Water depth is also greater at the C12 site than at the other mooring sites (60 m versus < 50 m; Table 1). Although currents at this site were correlated with local winds (r > 0.6; Table 2), differences in the winds at C12 compared to winds over the central Chukchi shelf likely lead to the reduction in correlation of the currents (Table 2, 3).

3.4 Re-examination of circulation pathways

Having described the general patterns of wind and currents in the region as well as their statistical relationships, we now turn to a more detailed examination of flow pathways on the eastern Chukchi shelf. A targeted view of bathymetry and flow patterns near the Central Channel is illustrated in Figure 10. The drifters were deployed in a number of different years and at different starting locations. Despite this, there is a marked and repeated eastward turning of drifters near 71.1 °N. In addition to the discussion presented by Stabeno et al. (2018), evidence of such a flow appears in other work. The first prior mention of such a flow is contained in Weingartner et al. (2005), who stated that the flow "bifurcates west of Hanna Shoal, with one branch continuing northeastward toward the slope and the other eastward along the southern flank of Hanna Shoal." Pickart et al. (2016) also cited "evidence of an offshoot from the Central Channel pathway". Pacini et al. (2019) presented hydrographic and velocity data collected south of the western part of Hanna Shoal (their Fig. 6b) that captured a bottom-intensified geostrophic current advecting dense water eastward out of Central Channel. An eastward flow near 71.1 °N also appears in the velocity compilations of Lin et al. (2019), in agreement with our drifter records. Their analysis indicates additional modulation of the shelf flows by the local wind field.

To further investigate this we examined a number of different bathymetry products including the ~400 m resolution SRTM15+V2.1 global elevation grid (Tozer et al. 2019), the ~200-m resolution International Bathymetric Chart of the Arctic Ocean version 4.0 (IBCAOv4.0; Jakobsson et al. 2020), the ~400-m resolution General Bathymetric Chart of the Oceans 2020 grid (GEBCO_2020; GEBCO Compilation Group, 2020), as well as the ~1-km resolution ARDEMv2.0 grid (Danielson et al. 2015). In this region, the SRTM15+V2.1 grid appeared noisy and contained erroneous depths near

shore, which was not surprising given that satellite-derived signals are lower quality in shallow water and over sandy bottoms such as on the Chukchi shelf (Tozer et al. 2019). The global GEBCO_2020 grid incorporates a large number of regional bathymetric products, including the IBCAOv4.0 product. Over the eastern Chukchi Sea shelf, the IBCAOv4.0 grid contains very few updates relative to its version 3 predecessor (Jakobsson et al. 2012, 2020). Notably the IBCAOv3.0 bathymetry is also part of the recent ARDEMv2.0 grid, but ARDEMv2.0 reportedly incorporates additional ship-based soundings and digitized historic nautical charts. Thus, ARDEMv2.0 and GEBCO_2020 currently contain the best publicly available bathymetry for the eastern Chukchi Sea.

Selected bathymetry contours from the ARDEMv2.0 grid near the Central Channel are drawn in Figure 10. A number of features stand out, including Central Channel and the deeper nearshore channel that continues northeast past the C1 mooring. Near 71.1 °N there is also a bathymetric depression that extends west from the C2 mooring to Central Channel. To the south of this depression near 70.8 °N, 164.5 °W, a fairly substantial shoal exists as marked by the 35-m depth contour. Both the depression and the shoal are reasonably large, with length scales >40 km. Interestingly, the drifters that turn east tend to do so near the bathymetric depression at 71.1 °N and move eastward north of the shoal. We note that similar bathymetric features also exist in the GEBCO_2020 grid, although since it and the ARDEMv2.0 grid both contain IBCAO bathymetry, they are not independent.

The bathymetric relief in this region is admittedly small. Nevertheless, multiple drifters moving northeastward through Central Channel divert eastward near the two bathymetric depressions (toward C1 and C2). The remainder of the flow moving northwestward in Central Channel diverts northward along Hanna Shoal. It is clear from an examination of the drifter data here and in Stabeno et al. (2018) that, after branching eastward off Central Channel, the flow continues past C1 and C2 and onward toward the head of Barrow Canyon where it exits into the Beaufort Sea.

3.5 Transport

3.5.1 Icy Cape Transport

Data from the three moorings deployed off Icy Cape (C1, C2, and C3; Fig. 1) are used to form an estimate of volume transport along the Chukchi shelf. The calculation follows methods described previously (Schumacher et al. 1989; Stabeno et al. 1995, 2016a, 2018). Briefly, the component of velocity normal to the line spanning the three moorings was first filled uniformly to the surface and bottom boundaries. Those velocity records were then multiplied by the cross-sectional areas defined by midpoints between moorings and designated shoreward and offshore limits. Each of the three resulting transport estimates was then summed to form an estimate of total transport along the eastern portion of the shelf.

As discussed by Stabeno et al. (2018) there are a number of errors inherent in this calculation including: measurement errors; errors resulting from unsampled near-surface and bottom velocities; accuracy of the shelf-wide estimates constructed from only three mooring sites; and finally errors pertaining to lateral coverage beyond the three-mooring array. In the region spanned by the moorings, the Chukchi shelf is reasonably flat and velocities at the three mooring sites are highly correlated in the vertical (see Table 2 of Stabeno et al. 2018), providing confidence in the vertical extrapolation. Similarly, currents at the three sites are horizontally well correlated (Table 3; Stabeno et al. 2018), suggesting that the mooring array captures a meaningful representation of shelf-wide flows. Weingartner et al. (2005) arrived at a similar conclusion after analyzing data from their own Chukchi shelf moorings. We thus believe the largest source of error in the transport estimate lies in the unsampled regions just outside of the array, between C1 and the coast, and offshore of the C3 mooring.

Following Stabeno et al. (2018) we chose the 40-m isobath as the shoreward boundary for our transport estimate. Support for this choice can be found in Pickart et al. (2016) and Lin et al. (2019). A cross-shelf CTD transect occupied near Icy Cape to the 25-m isobath in 2010 suggested that the highest geostrophic velocities were associated with the coastal jet between the 35- and 45-m isobaths, or centered near ~40 m, and decreased inshore of the 35-m isobath (Pickart et al. 2016, their Figures 7a and 9). Close to the coast, we expect bottom friction to dampen flows considerably, so this shoreward weakening of the along-shelf flow seems reasonable. A composite view of vertically averaged flow vectors throughout the eastern Chukchi also indicates that the largest

velocities off Icy Cape are centered near the 40-m isobath (Lin et al. 2019) with weaker velocities nearer to the coast, in agreement with Pickart et al. (2016). Using the C1 velocity record as representative of shelf flows to the 40-m isobath therefore seems reasonable. We note that some portion of the remaining very nearshore region contains landfast ice for a significant part of the year (Sullivan et al., this issues), which would further restrict transport. Nevertheless, if we assume the velocities at C1 extend throughout the quasi-triangular region bounded by the shore, then our transport estimate would increase by an average of ~10%. Given the aforementioned velocity decrease shoreward of the 35-m isobath, landfast ice during winter, and episodic nearshore wind-driven reversals (Fang et al., 2017; Pacini et al. 2019), we expect actual errors associated with unobserved nearshore flows to be less than ~10%.

Stabeno et al. (2018) took the offshore limit for their transport estimate as half of the distance between the two outermost moorings (C2 and C3), seaward of C3. That distance would place the outer influence of C3 just shoreward of the 50-m isobath. As with the unobserved nearshore flows, at least some observational evidence exists to help inform this choice. A cross-slope section east of Herald Canyon suggests that eastward flow remains over the shelf, confined largely shoreward of the ~60-m isobath (Fig. 16 of Pickart et al. 2010). A nearby absolute geostrophic velocity transect indicates that the zero velocity contour occurs at roughly the 50–55 m isobath (Fig. 7b of Pickart et al., 2016), and this appears to agree with the shipboard ADCP depth-averaged velocities of Pacini et al. (2019). Thus, the available observational evidence suggests that northeastward flows at C3 are likely representative of conditions out to the 50-m isobath, and possibly even the 55-m isobath. Until additional time series records are obtained seaward of the C3 mooring, the choice of the 50-m isobath appears to be a reasonable offshore bound for the transport estimate.

Using the argument above, C1 is representative of the area between the 40-m isobath and half the distance to the C2 mooring, or 60 km. Similarly, C2 spans 73 km (half the distance to C1 plus half the distance to C3). Finally, C3 spans 92 km (half the distance to C2 plus the distance to the 50-m isobath).

The temporal evolution of monthly averaged transport past the Icy Cape section is illustrated in Figure 11. We calculate both the monthly mean transport ($T_{1,2,3}$) using C1,

C2 and C3 and also the transport ($T_{1,2}$) through just C1 and C2. Not surprising, the time series are highly correlated and $T_{1,2}$ is ~60% of $T_{1,2,3}$. Two features are prominent: first, a seasonal cycle is clearly evident through February 2016, but is absent in later years; and second, the transport appears to increase over the 9 year period by ~0.03 Sv per year (Fig. 11a), though the linear trend is not significant at the 95% level. Interestingly, this compares well to the upper range estimated for the Bering Strait transport by Woodgate (2018). Note that the difference in transport between $T_{1,2,3}$ and $T_{1,2}$ is largest during warm months and weakest during winter months (Fig. 11c).

$T_{1,2,3}$ typically varies from 0 to 1 Sv, though monthly mean values as low as -0.5 Sv and as high as 1.7 Sv were recorded. The nine-year average Icy Cape transport is 0.43 Sv, or ~40% of flow through Bering Strait. Highest transports are in the spring/summer months and lowest values occur in fall/winter, as dictated by seasonal changes in winds (Stabeno et al., 2018). A more detailed illustration of the monthly values is provided in Figure 12. The mean monthly average (2010–2019) shows a distinct temporal pattern (Fig. 12a). The variability (standard deviation of the monthly means) from October through March is large, ranging from 0.4 to 0.6 Sv, while in spring and summer it is on average much smaller (Fig. 12a). The highest mean transport is in July. The variability in transport is evident in Figure 12b, with more negative (blue) transports in early years during fall/winter and fewer in the later years.

3.5.2 Central Channel Transport

An estimate of transport through Central Channel was made following the same approach outlined above for Icy Cape, applied to the C10 and C11 moorings (Fig. 1). Initially, the outer limits of the cross-sectional area were taken as the 45-m isobath on each side of the mooring pair, instead of extending the section by the half-distance between the C10 and C11 moorings. This choice better constrains the transport to that actually flowing down Central Channel. A closer examination of the drogued drifter tracks (Fig. 4), however, suggested a wider width was likely appropriate since drifters outside of the 45-m isobath limits continued transiting down Central Channel. To be comparable to the Icy Cape transports which were bounded by 40-m isobath, we used ~40-m isobath for this calculation also.

The resulting annual average of transport through the Central Channel section occupied by the C10 and C11 moorings varied from 0.46–0.55 Sv (Table 4), which was slightly less than transport at Icy Cape each year. In addition, the transport through Central Channel was highly correlated with the transport at Icy Cape, with correlation coefficients $r^2 > 0.88$ (Table 4). Even though there is good agreement between depth-averaged velocity records at the individual mooring sites (Table 3) and broad spatial coherence of the wind field (Fig. 4), the high transport correlations and similar magnitudes (Table 4; Fig. 13) remain surprising. Considering the high transport correlations and similar magnitudes between Icy Cape and Central Channel (Fig. 13), along with evidence of an eastward turning of the Central Channel flow between 71 and 72 °N from the drogued drifter tracks (Fig. 5), suggests that much of the Central Channel flow passing the C10 and C11 moorings actually turns to flow past the Icy Cape transect before exiting the shelf via Barrow Canyon.

4 Summary and Conclusions

Updated velocity records from previously occupied sites on the northeast Chukchi continental shelf and new records from previously unoccupied sites confirm that shelf flows are highly correlated in space and vertically throughout the interior water column. Comparisons with winds from a recent atmospheric reanalysis product (ERA5) similarly confirm high wind-current correlations with variations in winds leading current variability by 7–17 hours.

The moored current meter records agree well with patterns of flow delineated from satellite-tracked drifters. The eastern branch of Pacific-origin water generally flows north from Bering Strait passing Point Hope. The two historical branches of an enhanced flow near the coast and a separate flow that continues north through Central Channel each appear in the mooring and drifter data sets. Drogued drifter data also indicate the presence of a persistent flow out of Central Channel, turning east near 71.1 °N, that continues past Icy Cape and then out Barrow Canyon. The transport through Central Channel was highly correlated with transport past Icy Cape and was similar in magnitude. This lends additional support that a significant portion of the flow in Central Channel travels eastward *via* seafloor depressions and joins the Alaskan Coastal Current.

At present it remains unclear just how accurate the bathymetry is in this region and whether or not the seafloor depression and unnamed shoal actually exist. It is possible that the features are simply artifacts of erroneous data. The evidence provided by the drifter motions suggest that the features are, in fact, real. In any case, it is clear that a dedicated field-based examination of both the bathymetry and the circulation in the region is sorely needed.

The additional velocity records presented here allowed for an extension in time of the shelf-wide volume transport past Icy Cape to nine years. With the chosen bounds shoreward of the C1 mooring and seaward of the C3 mooring, the transport at Icy Cape accounts for ~40% of northward transport through Bering Strait similar to that reported in Stabeno et al. (2018). A seasonal cycle is also evident in the volume transport record with highest, least variable transports occurring in the summer months when winds are weakest, and lowest, and highly variable, transports occurring in fall/winter months when opposing winds are strongest. Aside from the seasonal variability, a positive, although not significant, linear trend of ~0.03 Sv per year exists over the entire 9-year record. Since the Pacific-origin water that flows north over the Chukchi shelf in route to the Arctic Basin carries a substantial amount of heat, freshwater, and nutrients, continued monitoring of this shelf system will help us to better understand ongoing changes.

Acknowledgements

We thank G. Lebon, D. Strausz, and S. Bell for collection and analysis of the data, and the officers and crews of the NOAA Ship *Oscar Dyson*, R/V *Thomas G. Thompson*, and USCGC *Healy* for invaluable assistance in obtaining these oceanographic measurements. This research was supported in part through the North Pacific Research Board (NPRB) Arctic Integrated Ecosystem Research Program (IERP; Baker et al., 2020; http://www.nprb.org/arctic-program/), as well as NOAA's North Pacific Climate Regimes and Ecosystem Productivity program, NOAA's Arctic Research programs and BOEM. Comments from three anonymous reviewers improved the manuscript. This is NOAA PMEL Contribution #5354, EcoFOCI Contribution #1025, and is NPRB Publication Number Arctic IERP-21. The statements, findings, conclusions, and

recommendations are those of the authors and do not reflect the views of NOAA or the Department of Commerce.

Table 1. Mooring name, location and water depth are indicated in the first column. All sites had a 300 or 600 kHz ADCP except for C1 in 2016, at which the ADCP failed and data from a SeaGuard are used. The second column gives the deployment period. Near bottom measurements were used to calculate maximum speed from hourly velocities; net speed and principal axis calculated from the low-pass filtered data (35-hr Lancos).

Mooring	Dates	Max Speed ($cm\ s^{-1}$)	Net speed (Dir) ($cm\ s^{-1}$, °)	Prin. Axis (% var) (° , %)
C1 (43 m)	9/15/2016-8/9/2017	60	10.1, 40	47, 87
70.84°N	8/9/2017-8/14/2018	90	9.2, 76	66, 88
163.13°W	8/14/2018-8/18/2019	68	8.7, 90	69, 91
C2 (42 m)	9/14/2016-8/8/2017	48	8.0, 100	106, 66
71.21°N	8/8/2017-8/13/2018	75	7.3, 108	118, 62
164.22°W	8/13/2018-8/14/2019	53	6.7, 97	88, 71
C3 (44 m)	9/14/2016-8/20/2017	42	5.9, 66	66, 65
71.82°N	8/20/2017-8/12/2018	52	7.2, 65	66, 65
166.06°W	8/12/2018-8/13/2019	47	5.6, 66	57, 67
C4 (47 m)	9/7/2016-8/15/2018	80	14.2, 100	86, 88
71.04°N	8/12/2017-8/15/2018	119	9.3, 108	80, 91
160.50°W	8/15/2018-8/19/2019	101	11.5, 100	81, 91
C5 (47 m)	9/7/2016-8/12/2017	98	14.3, 62	72, 92
71.21°N	8/12/2017-8/16/2018	103	9.3, 107	79, 91
158.02°W	8/16/2018-8/20/2019	132	12.6, 69	80,92
C10 (47 m)	9/19/2016-8/7/2017	51	10.1, 20	26, 87
70.22°N	8/7/2017-8/12/2018	58	10.4, 16	30, 87
167.79°W	8/12/2018-8/12/2019	63	8.0, 33	34, 90
C11 (46 m)	9/19/2016-8/7/2017	54	9.0, 40	47, 87
70.02°N	8/7/2017-8/11/2018	69	9.1, 62	63, 87
166.85°W	8/11/2018-8/12/2019	57	7.9, 38	38, 91
C12 (60 m)	9/21/2016-8/23/2017	73	11.1, 337	325, 87
67.91°N	8/23/2017-8/11/2018	67	10.9, 334	327, 86
168.19°W	8/11/2018-8/11/2019	75	8.4, 336	327, 87

Table 2. Lagged complex (vector) correlations between the local ERA5 winds and local bottom currents at 8 moorings deployed in 2016–2018. Correlation amplitudes are denoted r. Positive/negative angles (°) indicate that currents are rotated counterclockwise/clockwise from the wind, respectively. Positive lag (hrs) indicates that winds lead currents by the quantity shown.

Mooring	2016 Deployment			2017 Deployment			2018 Deployment		
	r	°	lag (hr)	r	°	lag (hr)	r	°	lag (hr)
C1	0.48	7	8	0.58	-16	13	0.59	-25	9
C2	0.41	-59	17	0.55	-67	17	0.58	-58	13
C3	0.48	-52	13	0.54	-66	12	0.55	-50	11
C4	0.49	-22	13	0.60	-20	12	0.58	-27	10
C5	0.55	-14	12	0.59	-15	8	0.59	-27	8
C10	0.46	4	14	0.49	-1	14	0.60	-8	9
C11	0.49	-4	11	0.49	-29	14	0.59	-6	9
C12	0.61	35	7	0.61	41	10	0.70	43	10

Table 3. Zero-lag vector correlations among the various bottom currents from moorings deployed in 2016 (top panel), 2017 (middle), and 2018 (bottom). Lower left section contains the correlation amplitudes, and the upper right contains the angle between the two vector time series. Positive/negative angle indicates that currents at sites in the left column are rotated counterclockwise/clockwise from currents at sites in other columns.

2016	C1	C2	C3	C4	C5	C10	C11	C12
C1		54	38	38	31	-23	-9	-95
C2	0.54		-14	-12	-30	-58	-27	-120
C3	0.48	0.72		3	-10	-38	-17	-93
C4	0.79	0.79	0.62		-12	-55	-32	-129
C5	0.82	0.68	0.58	0.88		-46	-27	-116
C10	0.77	0.61	0.64	0.74	0.70		-19	-59
C11	0.74	0.55	0.50	0.67	0.63	0.88		-72
C12	0.45	0.38	0.41	0.49	0.41	0.49	0.44	

2017	C1	C2	C3	C4	C5	C10	C11	C12
C1		27	15	7	7	-29	5	-95
C2	0.79		-10	-28	-34	-50	-7	-106
C3	0.62	0.70		-13	-17	-35	7	-85
C4	0.89	0.76	0.55		-4	-42	-8	-122
C5	0.78	0.66	0.46	0.88		-47	-15	-128
C10	0.76	0.56	0.6	0.65	0.57		31	-60
C11	0.72	0.51	0.55	0.57	0.51	0.87		-87
C12	0.44	0.24	0.42	0.37	0.34	0.59	0.61	

2018	C1	C2	C3	C4	C5	C10	C11	C12
C1		17	3	8	10	-31	-27	-98
C2	0.87		-13	-12	-12	-42	-36	-107
C3	0.64	0.73		3	5	-24	-21	-94
C4	0.91	0.82	0.59		-1	-41	-38	-110
C5	0.85	0.74	0.57	0.90		-46	-43	-113
C10	0.80	0.70	0.66	0.70	0.69		4	-64
C11	0.80	0.68	0.59	0.69	0.67	0.92		-65
C12	0.68	0.61	0.53	0.64	0.59	0.70	0.69	

Table 4. Statistics for the transport calculated in Central Channel (using time series C11 and C12) and Icy Cape (using time series C1, C2, and C3).

	Icy Cape Mean ± std	Central Channel Mean ± std	Correlation (r^2)
2016-2017	0.63 ± 0.75	0.55 ± 0.64	0.83
2017-2018	0.59 ± 0.94	0.53± 0.73	0.83
2018-2019	0.52 ± 0.95	0.48 ± 0.76	0.87

References

Baker, M.R., Farley, E.V., Ladd, C., Danielson, S.L., Stafford, K.M., Huntington, H.P., Dickson, D.M., 2020. Integrated ecosystem research in the Pacific Arctic–understanding ecosystem processes, timing and change. Deep-Sea Res. II 177, 104850. https://doi.org/10.1016/j.dsr2.2020.104850.

Carmack, E., and Wassman, P. 2006. Food webs and physical-biological coupling on pan-Arctic shelves: Unifying concepts and comprehensive perspectives. Progress in Oceanography, 71: 446– 477.

Coachman, L.K., Aagaard, K., Tripp, R.B., 1975. Bering Strait: The Regional Physical Oceanography, Univ. of Washington Press, Seattle, Wash.

Corlett, W.B., Pickart, R.S., 2017. The Chukchi slope current. Prog. Oceanogr. 153, 50–65. https://doi.org/10.1016/j.pocean.2017.04.005.

Belmonte Rivas, M., and Stoffelen, A., 2019. Characterizing ERA-Interim and ERA5 surface wind biases using ASCAT. Ocean Sci. 15, 831–852, https://doi.org/10.5194/os-15-831-2019.

Danielson, S. L., Weingartner, T.J., Hedstrom, K.S., Aagaard, K., Woodgate, R., Curchitser, E., Stabeno, P.J., 2014. Coupled wind-forced controls of the Bering-Chukchi shelf circulation and the Bering Strait throughflow: Ekman transport, continental shelf waves, and variations of the Pacific-Arctic sea surface height gradient. Prog. Oceanogr. 125, 40–61. https://doi.org/10.1016/j.pocean.2014.04.006.

Danielson, S.L., Dobbins, E.L., Jakobsson, M., Johnson, M.A., Weingartner, T.J., Williams, W.J., Zarayskaya, Y., 2015. Sounding the northern seas. Eos, 96, https://doi.org/10.1029/2015EO040975.

Danielson, S.L., Eisner, L., Ladd, C., Mordy, C., Sousa, L., Weingartner, T.J., 2017. A comparison between late summer 2012 and 2013 water masses, macronutrients, and phytoplankton standing crops in the northern Bering and Chukchi Seas. Deep Sea Res. II, 135, 7–26, https://doi.org/10.1016/j.dsr2.2016.05.024.

Danielson, S., Ahkinga, O., Ashjian, C., Basyuk, E., Cooper, L.W., Eisner, L., Farley, E., Iken, K.B., Grebmeier, J.M., Juranek, L., Khen, G., Jayne, S., Kikuchi, T., Ladd, C., Lu, K., McCabe, R.M., Moore, G.W.K., Nishino, S., Okkonen, S.R., Ozenna, F., Pickart, R.S., Polyakov, I., Stabeno, P.J., Wood, K., Williams, W.J., Woodgate, R.A.,

Weingartner, T.J., 2020. Manifestation and consequences of Arctic amplification in the Bering and Chukchi Seas, Deep Sea Res. II, 177, https://doi.org/10.1016/j.dsr2.2020.104781.

Dee, D.P., Uppala, S.M., Simmons, A.J., Berrisford, P., Poli, P., Kobayashi, S., Andrae, U., Balmaseda, M.A., Balsamo, G., Bauer, P., Bechtold, P., Beljaars, A.C.M., van de Berg, L., Bidlot, J., Bormann, N., Delsol, C., Dragani, R., Fuentes, M., Geer, A.J., Haimberger, L., Healy, S.B., Hersbach, H., Hólm, E.V., Isaksen, L., Kållberg, P., Köhler, M., Matricardi, M., Mcnally, A.P., Monge-Sanz, B.M., Morcrette, J.J., Park, B.K., Peubey, C., de Rosnay, P., Tavolato, C., Thépaut, J.N., Vitart, F.,2011. The ERA-Interim reanalysis: configuration and performance of the data assimilation system. Q. J. Roy. Meteorol. Soc., 137, 553–597. https://doi.org/10.1002/qj.828.

Fang, Y.-C., Potter, R. A., Statscewich, H., Weingartner, T. J., Winsor, P., & Irving, B. K. (2017). Surface current patterns in the Northeastern Chukchi Sea and their response to wind forcing. Journal of Geophysical Research: Oceans, 122, 9530–9547. https://doi.org/10.1002/2017JC013121.

GEBCO Compilation Group 2020, 2020. The GEBCO_2020 Grid - a continuous terrain model of the global oceans and land. British Oceanographic Data Centre, National Oceanography Centre, NERC, UK. https://doi.org/10.5285/a29c5465-b138-234d-e053-6c86abc040b9.

Hersbach, H., B. Bell, P. Berrisford, S. Hirahara, A. Horanyi, J. Munoz-Sabater, J. Nicolas, C. Peubey, R. Radu, D. Schepers, A. Simmons, C. Soci, S. Abdalla, X. Abellan, G. Balsamo, P. Bechtold, G. Biavati, J. Bidlot, M. Bonavita, G. De Chiara, P. Dahlgren, D. Dee, M. Diamantakis, R. Dragani, J. Flemming, R. Forbes, M. Fuentes, A. Geer, L. Haimberger, S. Healy, R. J. Hogan, E. Holm, M. Janiskova, S. Keeley, P. Laloyaux, P. Lopez, C. Lupu, G. Radnoti, P. de Rosnay, I. Rozum, F. Vamborg, S. Villaume, J.-N. Thepaut. 2020. The ERA5 global reanalysis. Q. J. R. Meteorol. Soc. 146, 1999–2049. https://doi.org/10.1002/qj.3803.

Itoh, M., Nishino, S., Kawaguchi, Y., Kikuchi, T., 2013. Barrow Canyon volume, heat, and freshwater fluxes revealed by long-term mooring observations between 2000 and 2008. J. Geophys. Res. Oceans 118(9), 4363–4379. https://doi.org/10.1002/jgrc.20290.

Jakobsson, M. Mayer, L., Coakley, B., Dowdeswell, J.A., Forbes, S., Fridman, B., Hodnesdal, H., Noormets, R., Pedersen, R., Rebesco, M., Schenke, H.W., Zarayskaya, Y., Accettella, D., Armstrong, A., Anderson, R.M., Bienhoff, P., Camerlenghi, A., Church, I., Edwards, M., Gardner, J.V., Hall, J.K., Hell, B., Hestvik, O., Kristoffersen, Y., Marcussen, C., Mohammad, R., Mosher, D., Nghiem, S.V., Pedrosa, M.T., Travaglini, P.G., Weatherall, P., 2012. The International Bathymetric Chart of the Arctic Ocean (IBCAO) Version 3.0. Geophysical Research Letters. 39, L12609, https://doi.org/10.1029/2012gl052219.

Jakobsson, M., Mayer, L., Bringensparr, C., Castro, C., Mohammad, R., Johnson , P. Ketter, T., Accettella, D., Amblas, D., An, L., Arndt, J., Canals, M., Casamor, J., Chauche, N., Coakley, B., Danielson, S., Demarte, M., Dickson, M., Dorschel, B., Dowdeswell, J., Dreutter, S., Fremand, A., Gallant, D., Hall, J., Hehemann, L., Hodnesdal, H., Hong, J., Ivaldi, R., Kane, E., Klaucke, I., Krawczyk, D., Kristoffersen, Y., Kuipers, B., Millan, R., Masetti, G., Morlighem, M., Noormets, R., Prescott, M., Rebesco, M., Rignot, E., Semiletov, I., Tate, A., Travaglini, P., Velicogna, I., Weatherall, P., Weinrebe, W., Willis, J., Wood, M., Zarayskaya, Y., Zhang, T., Zimmermann, M., Zinglersen, K., 2020. The International Bathymetric Chart of the Arctic Ocean Version 4.0. Scientific Data. 7(176), https://doi.org/10.1038/s41597-020-0520-9.

Li, M., Pickart, R.S., Spall, M.A., Weingartner, T.J., Lin, P., Moore, G., Qi, Y., 2019. Circulation of the Chukchi Sea shelfbreak and slope from moored timeseries. Prog. Oceanogr. 172, 14–33. https://doi.org/10.1016/j.pocean.2019.01.002.

Lin, P., Pickart, R.S., McRaven, L.T., Arrigo, K.R., Bahr, F., Lowry, K.E., Stockwell, D.A., and Mordy, C.W., 2019. Water mass evolution and circulation of the northeastern Chukchi Sea in summer: implications for nutrient distributions. Journal of Geophysical Research: Oceans, 124, 4416–4432. https://doi.org/10.1029/2019JC015185.

Lin, P., Pickart, R.S., Vage, K., and Li, J., 2019. Fate of warm Pacific water in the Arctic Basin. Geophysical Research Letters, 48, e2021GL094693. https://doi.org/10.1029/2021GL094693.

Lindsay, R., Wensnahan, M., Schweiger, A., and Zhang, J., 2014. Evaluation of seven

different atmospheric reanalysis products in the Arctic. J. Climate 27, 2588–2606, https://doi.org/10.1175/JCLI-D-13-00014.1.

Mordy, C.W., Bell, S., Cokelet, E.D., Ladd, C., Lebon, G., Proctor, P., Stabeno, P., Strausz, D., Wisegarver, E., Wood, K., 2020. Seasonal and interannual variability of nitrate in the eastern Chukchi Sea: Transport and winter replenishment, Deep Sea Res. Part II, 177, https://doi.org/10.1016/j.dsr2.2020.104807.

Pacini, A., Moore, G.W.K., Pickart, R.S., Nobre, C., Bahr, F., Vage, K., Arrigo, K.R., 2019. Characteristics and transformation of Pacific Winter Water on the Chukchi Sea shelf in late spring. Journal of Geophysical Research: Oceans, 124, 7153–7177. https://doi.org/10.1029/2019JC015261.

Pickart, R.S., Pratt, L.J., Torres, D.J., Whitledge, T.E., Proshutinsky, A.Y., Aagaard, K., Agnew, T.A., Moore, G. W. K., Dail, H.J., 2010. Evolution and dynamics of the flow through Herald Canyon in the western Chukchi Sea. Deep-Sea Res. Part II 57(1–2), 5–26. https://doi.org/10.1016/ j.dsr2.2009.08.002.

Pickart, R.S., Moore, G.W.K., Mao, C., Bahr, F., Nobre, C., Weingartner, T.J., 2016. Circulation of winter water on the Chukchi shelf in early summer. Deep-Sea Research II, 130, 56–75. https://doi.org/10.1016/j.dsr2.2016.05.001.

Schumacher, J.D., Stabeno, P.J., and Roach, A.T., 1989. Volume transport in the Alaska Coastal Current. Cont. Shelf Res., 9 (12), 1071–1083.

Stabeno, P.J., Reed, R.K., Schumacher, J.D., 1995. The Alaska Coastal Current: Continuity of transport and forcing. J. Geophys. Res., 100, C2, 2477–2485.

Stabeno, P.J., Mordy, C.W., Sigler, M.F., 2020. Seasonal patterns of near-bottom chlorophyll fluorescence in the eastern Chukchi Sea: 2010–2019. Deep-Sea Res. Part II, 177. https://doi.org/10.1016/j.dsr2.2020.104842.

Stabeno, P.J. and R.M. McCabe, 2020. Vertical structure and temporal variability of currents over the Chukchi Sea continental slope. Deep-Sea Res. Part II, 177. https://doi.org/10.1016/j.dsr2.2020.104805

Stabeno, P.J., R.K. Reed, 1994. Circulation in the Bering Sea basin observed by satellite-tracked drifters: 1986–1993 J. Phys. Oceanogr., 24 (4), pp. 848–854

Stabeno, P.J., Bell, S., Cheng, W., Danielson, S., Kachel, N.B., Mordy, C.W., 2016a. Long-term observations of Alaska Coastal Current in the northern Gulf of

Alaska. *Deep-Sea Res. II*, *132*, 24–40, doi: 10.1016/j.dsr2.2015.12.016, Understanding Ecosystem Processes in the Gulf of Alaska: Volume 1.

Stabeno, P.J., Danielson, S.L., Kachel, D.G., Kachel, N.B., Mordy, C.W., 2016b. Currents and transport on the Eastern Bering Sea shelf: An integration of over 20 years of data. *Deep-Sea Res. II*, *134*, 13-29, https://doi.org/10.1016/j.dsr2.2016.05.010

Stabeno, P., Kachel, N., Ladd, C., Woodgate, R., 2018. Flow patterns in the eastern Chukchi Sea: 2010–2015. J. Geophys. Res. Oceans 123, 1177–1195. https://doi.org/10.1002/ 2017JC013135.

Sullivan, M. and Stabeno, P. this issue. A decade of measurements of ice draft in the Chukchi Sea

Tozer, B., Sandwell, D.T., Smith, W.H.F., Olson, C., Beale, J.R., Wessel, P., 2019. Global bathymetry and topography at 15 arc sec: SRTM15+. Earth and Space Science. 6, https://doi.org/10.1029/2019EA000658.

Tsukada, Y., Ueno, H., Ohta, N., Itoh, M., Watanabe, E., Kikuchi, T., Nishino, S., Mizobata, K., 2018. Interannual variation in solar heating in the Chukchi Sea, Arctic Ocean. Polar Science, 17, 33–39, https://doi.org/10.1016/j.polar.2018.06.003.

Watanabe, E., Onodera, J., Itoh, M., Nishino, S., Kikuchi, T., 2017. Winter transport of subsurface warm water toward the Arctic Chukchi Borderland. Deep-Sea Res. I, 128, 115–130, https://doi.org/10.1016/j.dsr.2017.08.009.

Weingartner, T., Aagaard, K., Woodgate, R., Danielson, S., Sasaki, Y., Cavalieri, D., 2005. Circulation on the north central Chukchi Sea shelf. Deep-Sea Res. Part II 52(24–26), 3150–3174. https://doi.org/10.1016/j.dsr2.2005.10.015.

Woodgate, R.A., 2018. Increases in the Pacific inflow to the Arctic from 1990 to 2015, and insights into seasonal trends and driving mechanisms from year-round Bering Strait mooring data. Prog. Oceanogr. 160, 124–154, https://doi.org/10.1016/j.pocean.2017.12.007.

Woodgate, R.A., Aagaard, K., Weingartner, T.J., 2005a. Monthly temperature, salinity, and transport variability of the Bering Strait through flow. Geophys. Res. Lett. 32, L04601. https://doi.org/10.1029/2004GL021880.

Woodgate, R.A., Aagaard, K., Weingartner, T.J., 2005b. A year in the physical oceanography of the Chukchi Sea: Moored measurements from autumn 1990–1991. Deep-Sea Res. Part II 52(24–26), 3116–3149. https://doi.org/10.1016/j.dsr2.2005.10.016.

Woodgate, R.A., Weingartner, T.J., Lindsay, R., 2012. Observed increases in Bering Strait oceanic fluxes from the Pacific to the Arctic from 2001 to 2011 and their impacts on the Arctic Ocean water column. Geophys. Res. Lett. 39, L24603. https://doi.org/10.1029/2012GL054092.

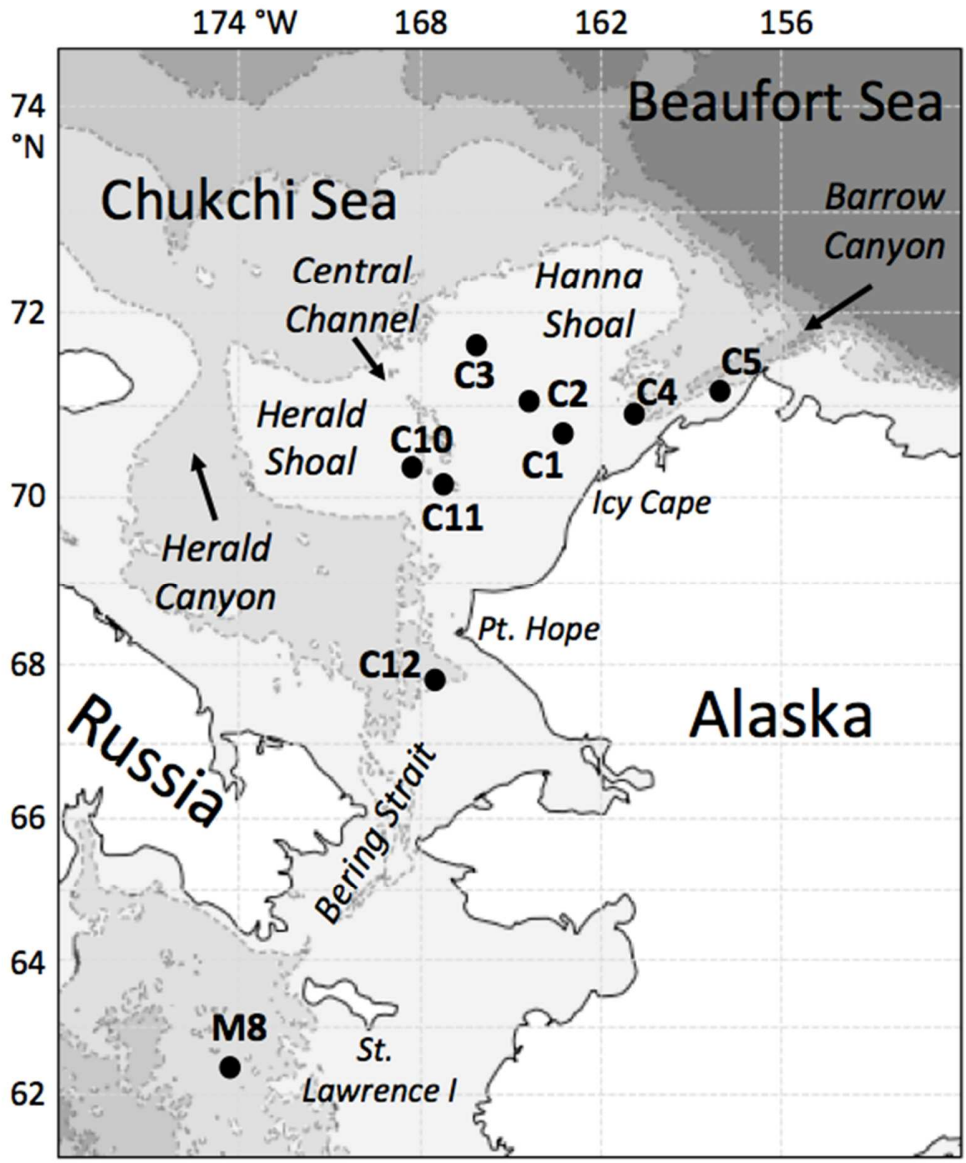

Figure 1: Geographic map of mooring locations in 2016– 2019 (black dots) in the northern Bering Sea and the Chukchi Sea.

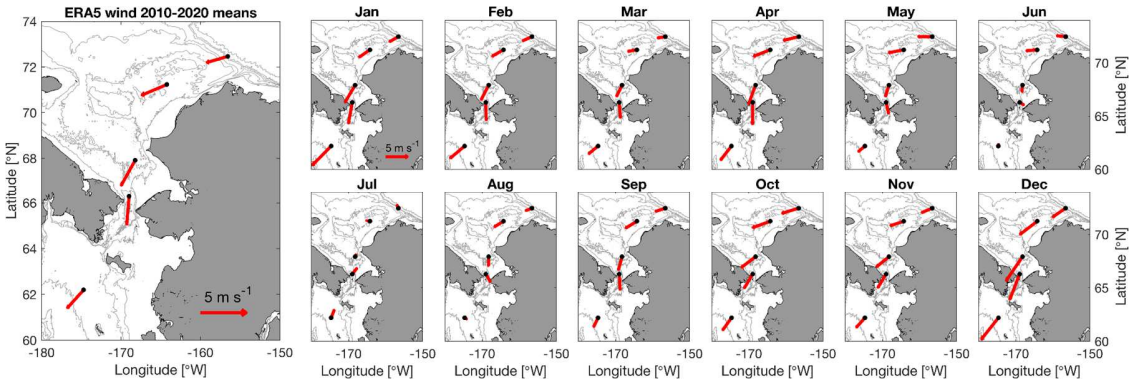

Figure 2: (left) 11-year mean ERA5 wind vectors (red) at select locations (black dots) in the northern Bering (M8, Fig. 1) and eastern Chukchi Seas. (right) Mean vectors for each month using the same 11-year data record. Wind vectors point in the direction the wind blows.

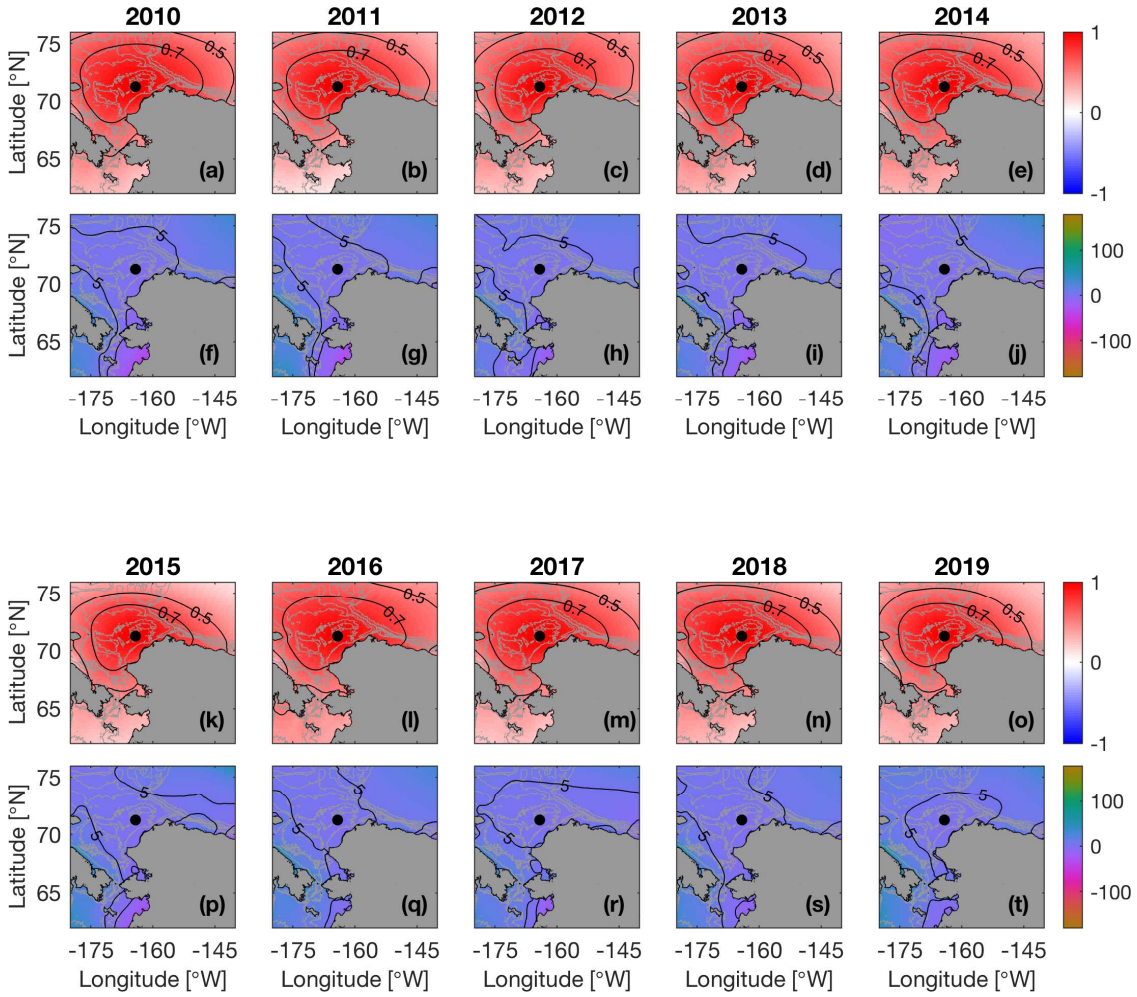

Figure 3: Yearly complex correlations of ERA5 wind vectors relative to a single point on the central Chukchi Sea shelf (black dot) from 2010–2019. Correlation amplitudes appear in panels (a–e), and (k–o); correlation phases appear in panels (f–j) and (p–t).

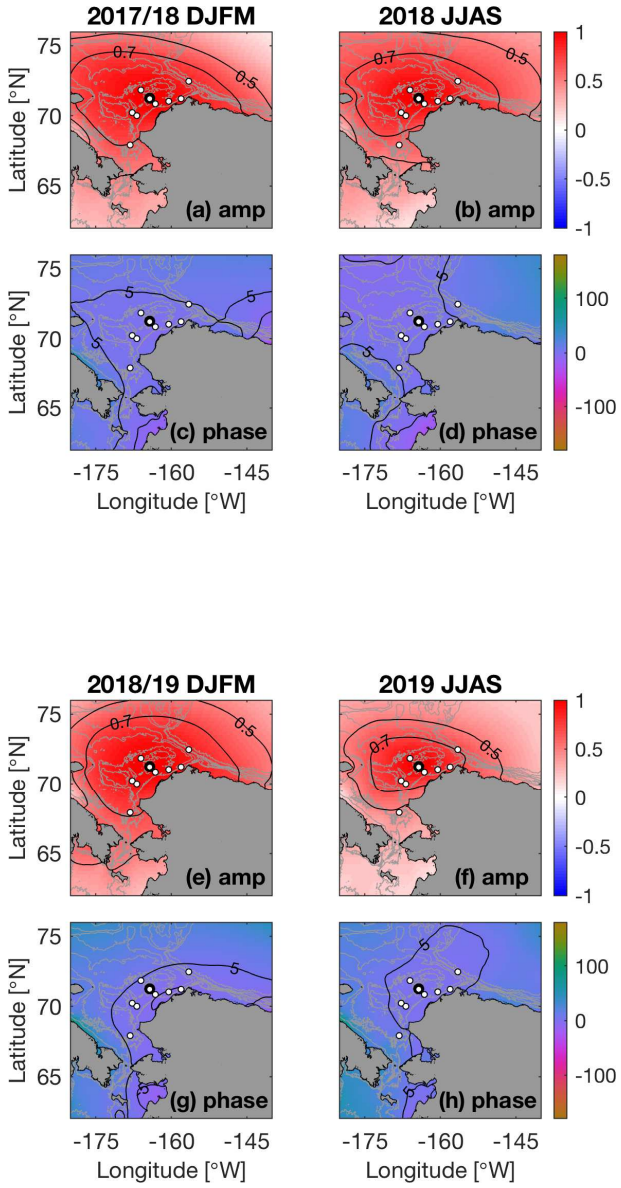

Figure 4: Seasonal complex correlations of ERA5 wind vectors relative to a single point on the central Chukchi Sea shelf (black dot) for the two most spatially extreme summer cases during 2010–2019. Correlation amplitudes appear in panels (a–b), and (e–f); correlation phases appear in panels (c–d) and (g–h). For comparison, left-side panels correspond to correlations from the preceding December–March (DJFM); right-side panels correspond to quantities spanning June–September (JJAS). The small white dots mark the primary mooring sites considered herein.

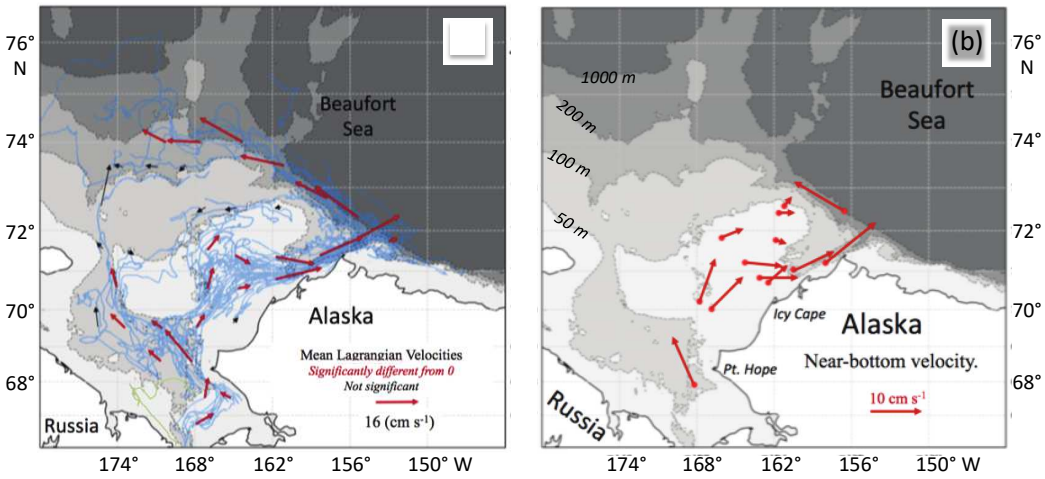

Figure 5: (a) Blue lines indicate trajectories of individual drifters (drogue depth ~30 m). Red and black vectors indicate the mean Lagrangian velocity of the drifters in each 1° latitude x 3° longitude box. The red arrows are significant velocities, while the black arrows are not. (b) Mean near bottom velocity from the moorings. In both panels the black contour represents the coastline. Bathymetry is gray and gradation changes appear at the 50, 100, 200, and 1000 m depths.

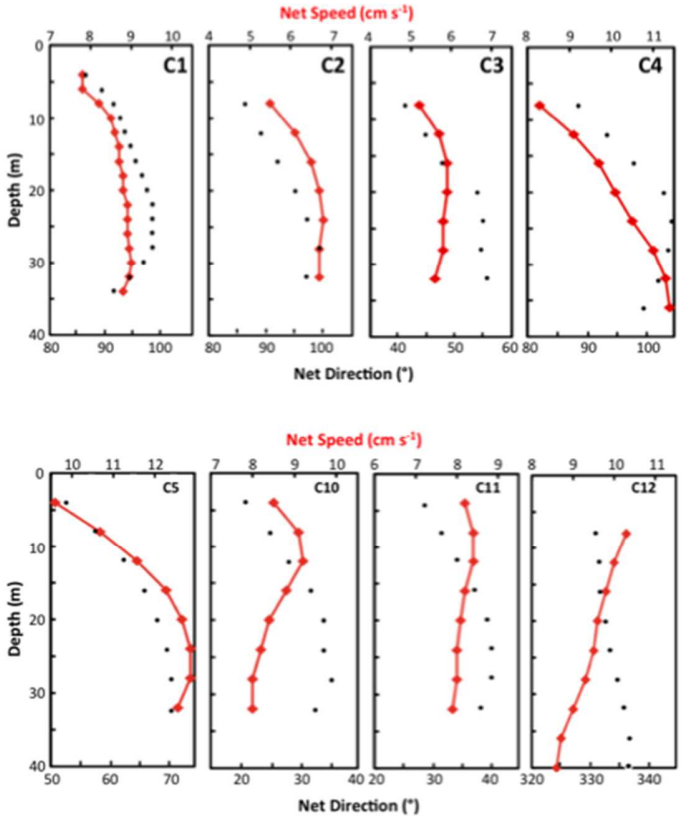

Figure 6: Annual mean vertical profiles of net speed (red) and direction (black) at each of the mooring sites on the Chukchi shelf for the 2018 deployments. To aid in comparisons, the aspect ratio is the same in each panel; the span of the x- and y-axes do not change from site to site. Refer to Fig. 1 for the mooring locations. Directions are relative to true north (°T).

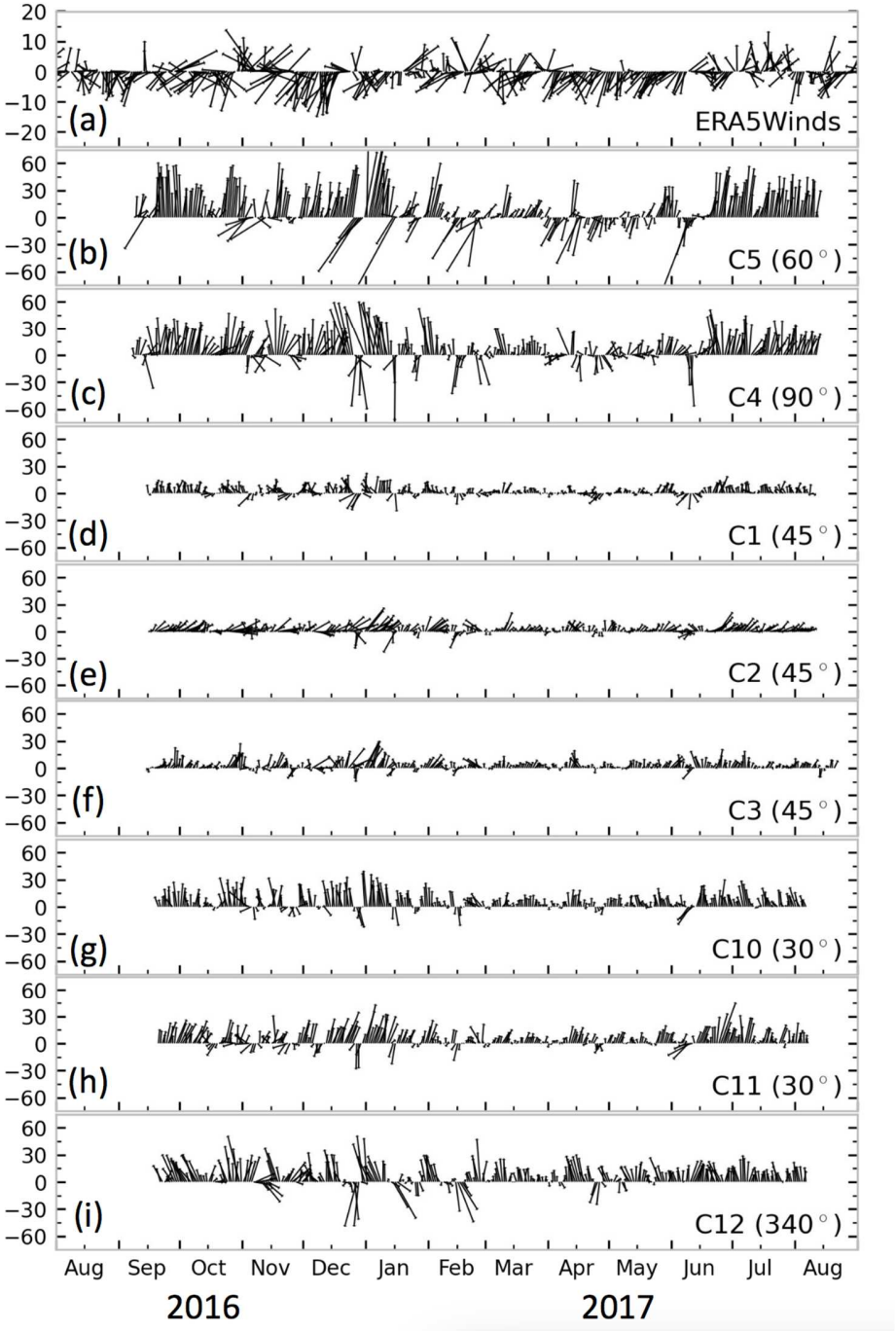

Figure 7: (a) Daily ERA5 wind vectors for September 2016 – August 2017. (b-i) Daily current vectors for September 2016 – August 2017. Time series of daily currents correspond to mooring sites (b) C5, (c) C4 (d) C1, (e) C2, (f) C3, (g) C10, (h) C11, and (i) C12. Vectors are rotated to the indicated angle relative to true north (°T).

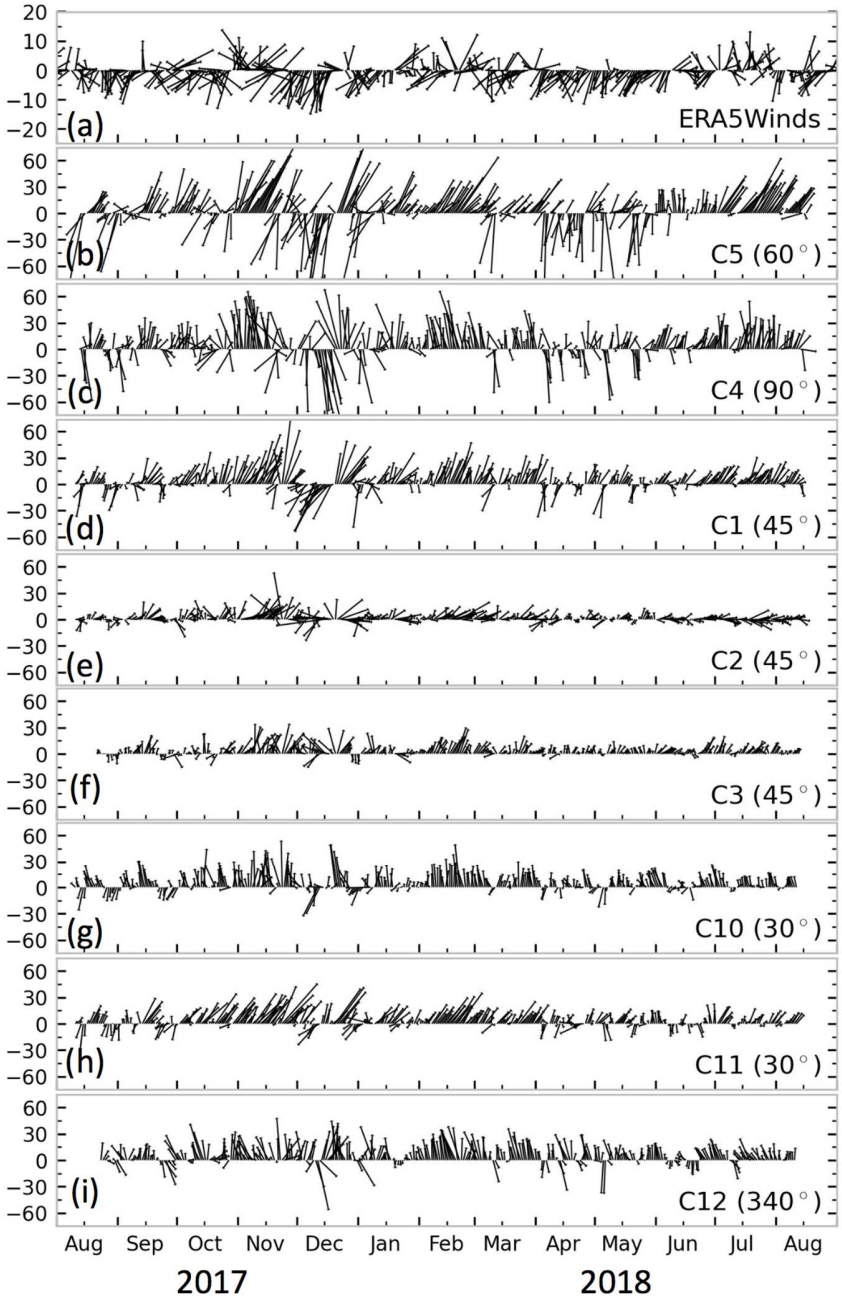

Figure 8: Same as Figure 7 except for August 2017 – August 2018.

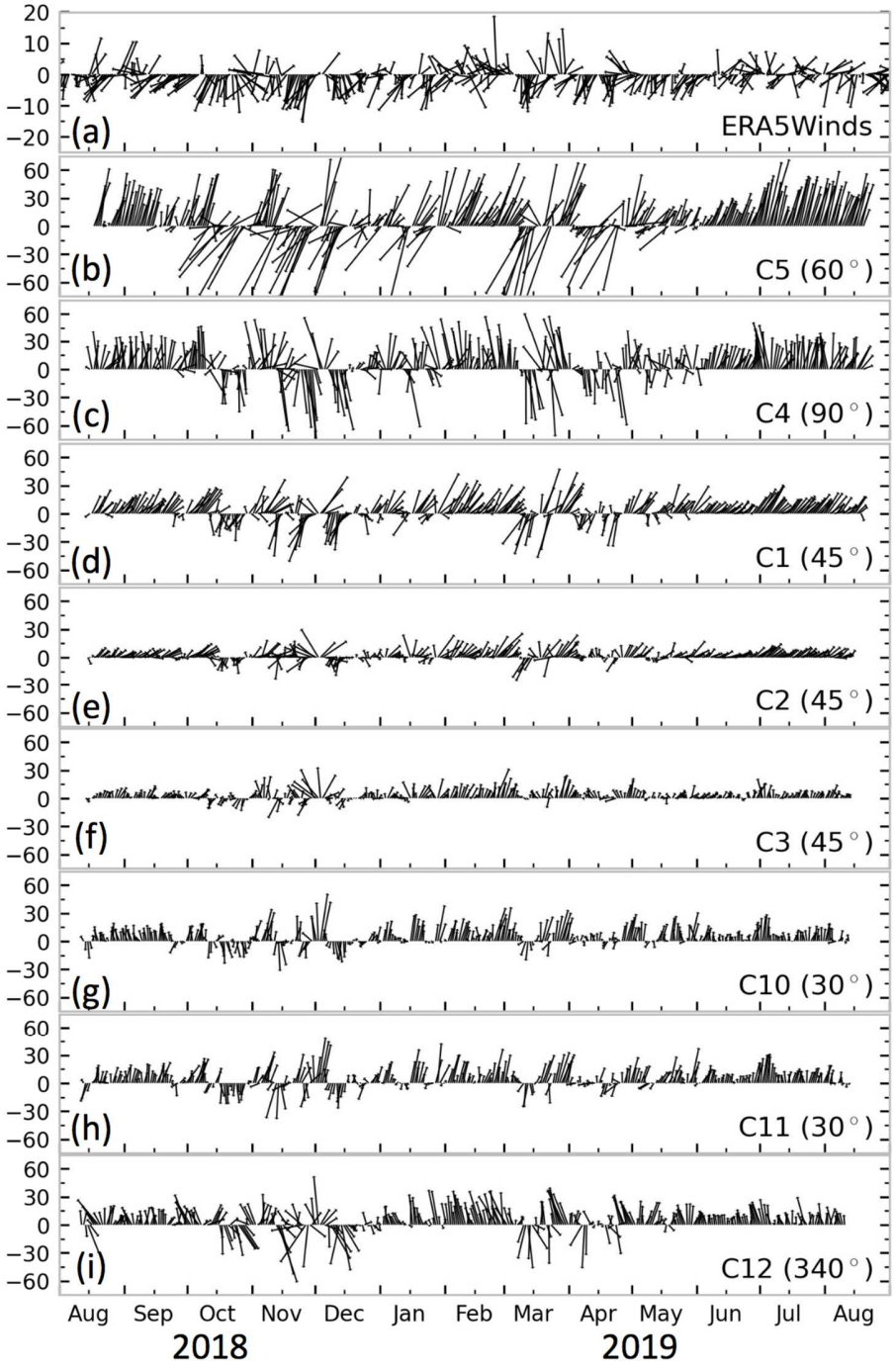

Figure 9: Same as Figure 7 except for August 2018 – August 2019.

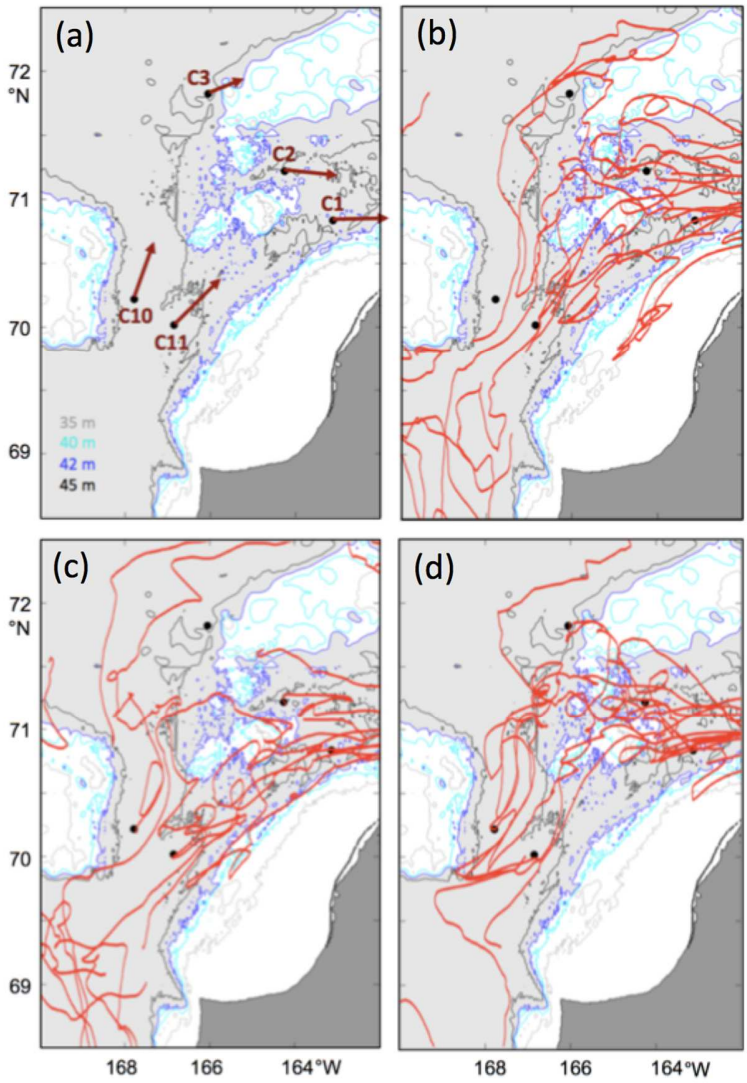

Figure 10: Zoomed view of bathymetry near Central Channel. The 35, 40, 42, and 45 m contours are colored; labels are shown in panel (a) . Land is shaded dark gray and depths > 42 m are shaded light gray. Black dots represent locations of the Central Channel (leftmost two; C10, C11) and Icy Cape (rightmost three; C1, C2, C3) moorings. Mean near-bottom flow vectors from the moorings are drawn red in (a), and select drifter tracks are drawn red in the remaining three panels, (b)-(d).

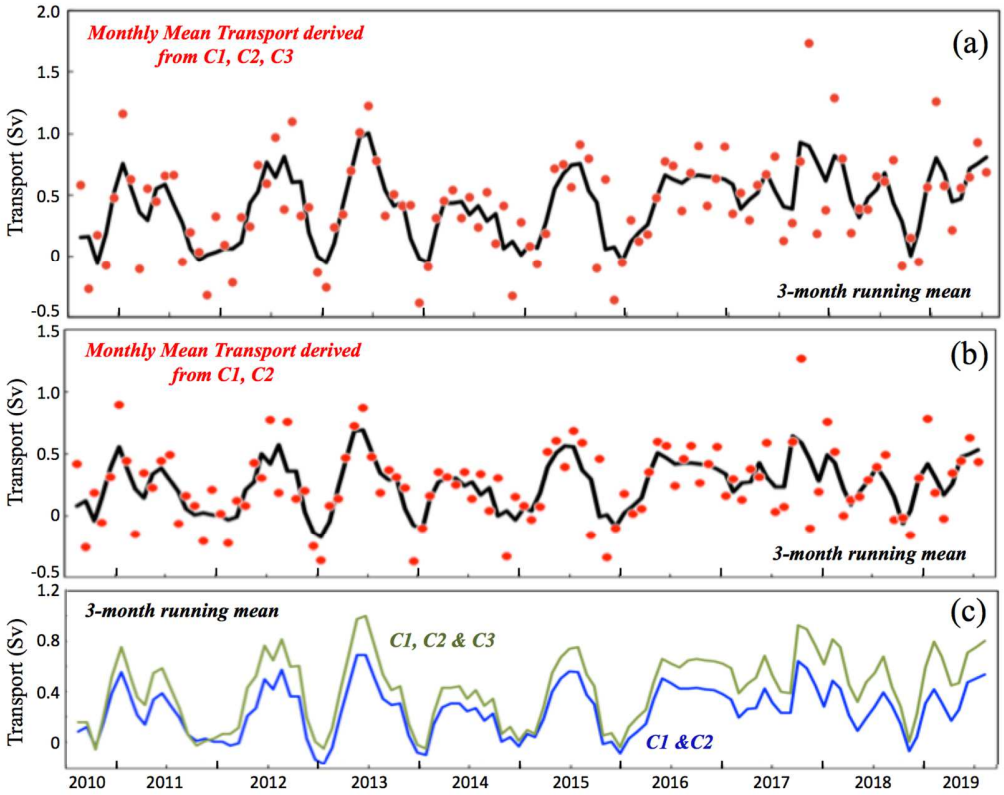

Figure 11. Monthly mean transport at Icy Cape (a) calculated from C1, C2 and C3, and (b) from just C1 and C2, excluding C3. (c) Comparison of transports shown in (a) and (b).

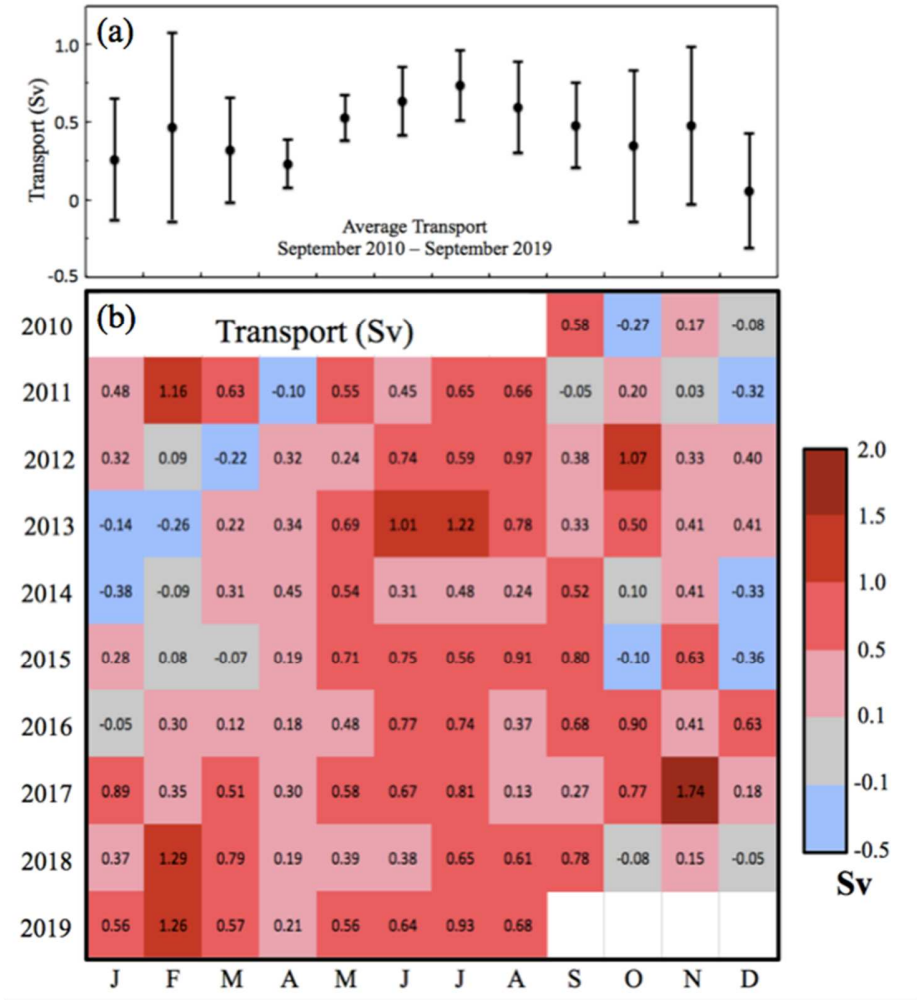

Figure 12. Monthly mean transport at Icy Cape calculated from C1, C2 and C3. (a) Mean and standard deviations of the monthly transports over the 9-year period, and (b) color coded transport (blue negative transport; red positive)

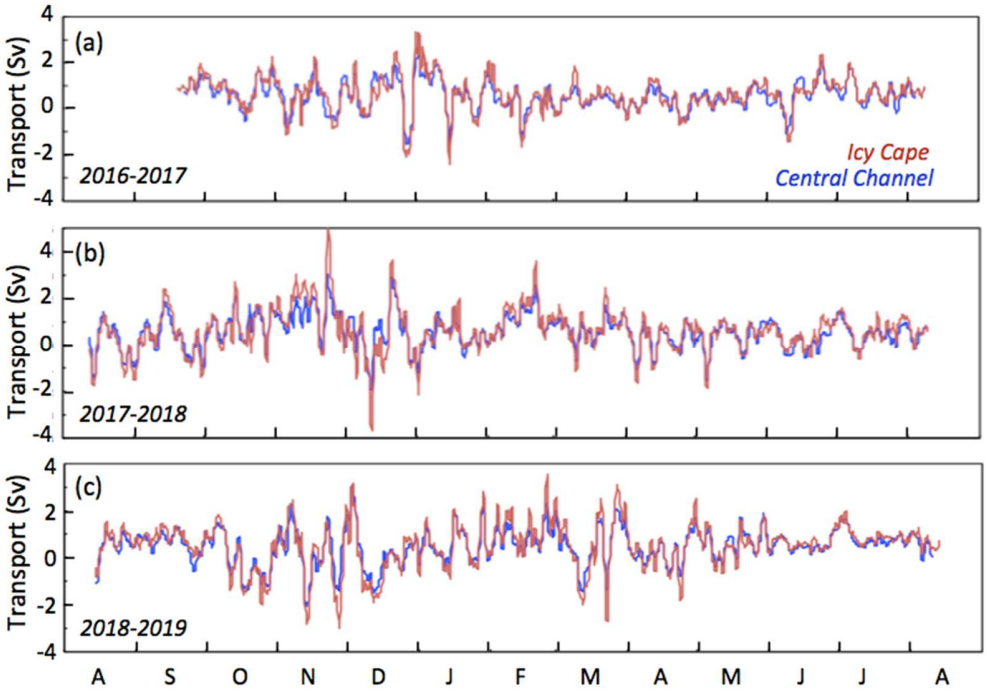

Figure 13. Time series of daily transport at Icy Cape (red) and Central Channel (blue) for three years.